Supplementary Information

1. Vorticity magnitude and helicity density field for helical vortex tube cases with different R/p and A

Fig. 1, printed over the next two pages, shows the vorticity magnitude and helicity density fields for cases with different values of R/p and $A = 3$ and $A = 4.3$, respectively. Each panel associated with a specific combination of parameters shows snapshots at six time instances showing the early phase, the first bursting event, and the bursting relaxation and twist wave reversal.

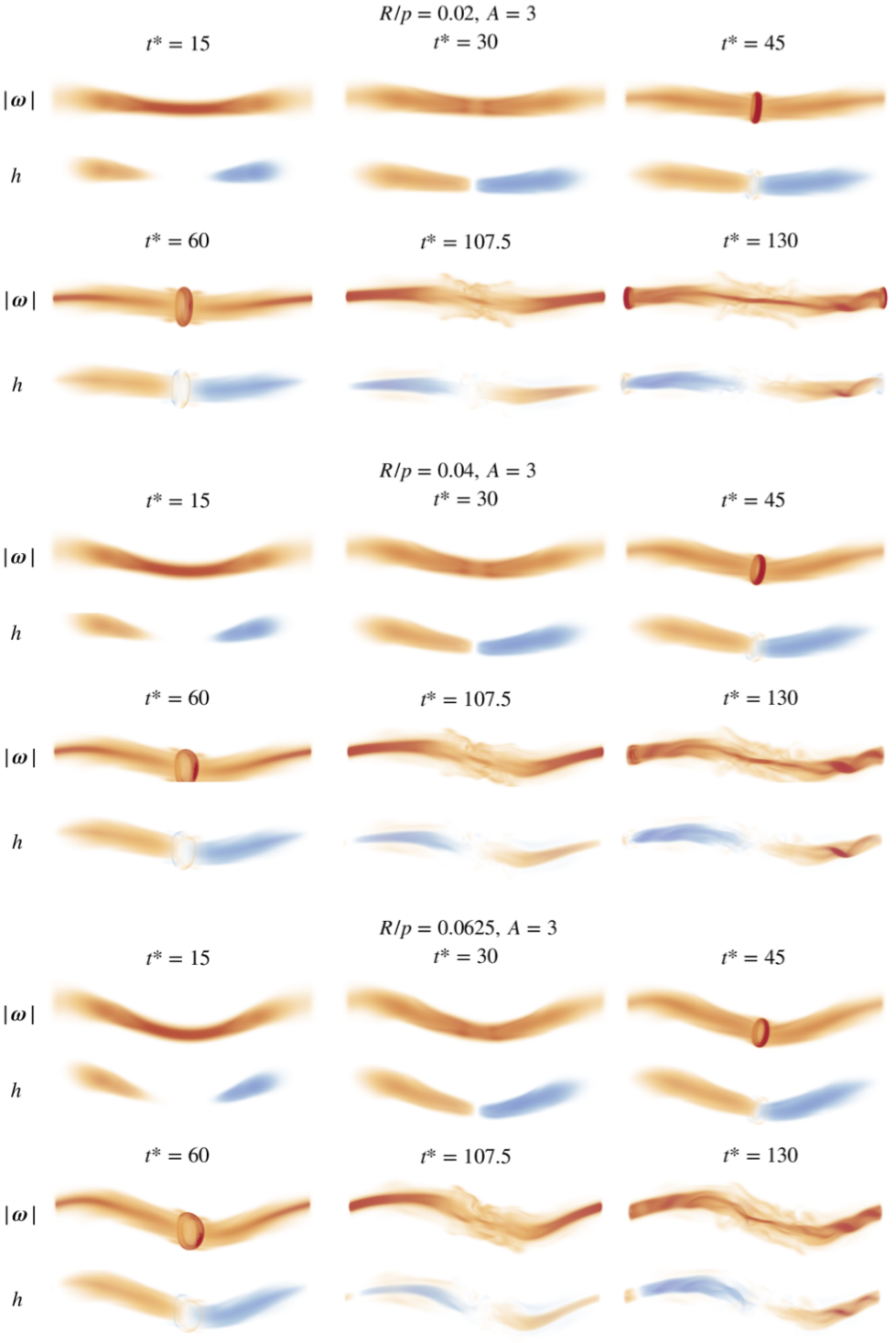
R/p = 0.02, A = 3
t* = 15
t* = 30
t* = 45
|ω|
h
t* = 60
t* = 107.5
t* = 130
|ω|
h
R/p = 0.04, A = 3
t* = 15
t* = 30
t* = 45
|ω|
h
t* = 60
t* = 107.5
t* = 130
|ω|
h
R/p = 0.0625, A = 3
t* = 15
t* = 30
t* = 45
|ω|
h
t* = 60
t* = 107.5
t* = 130
|ω|
h

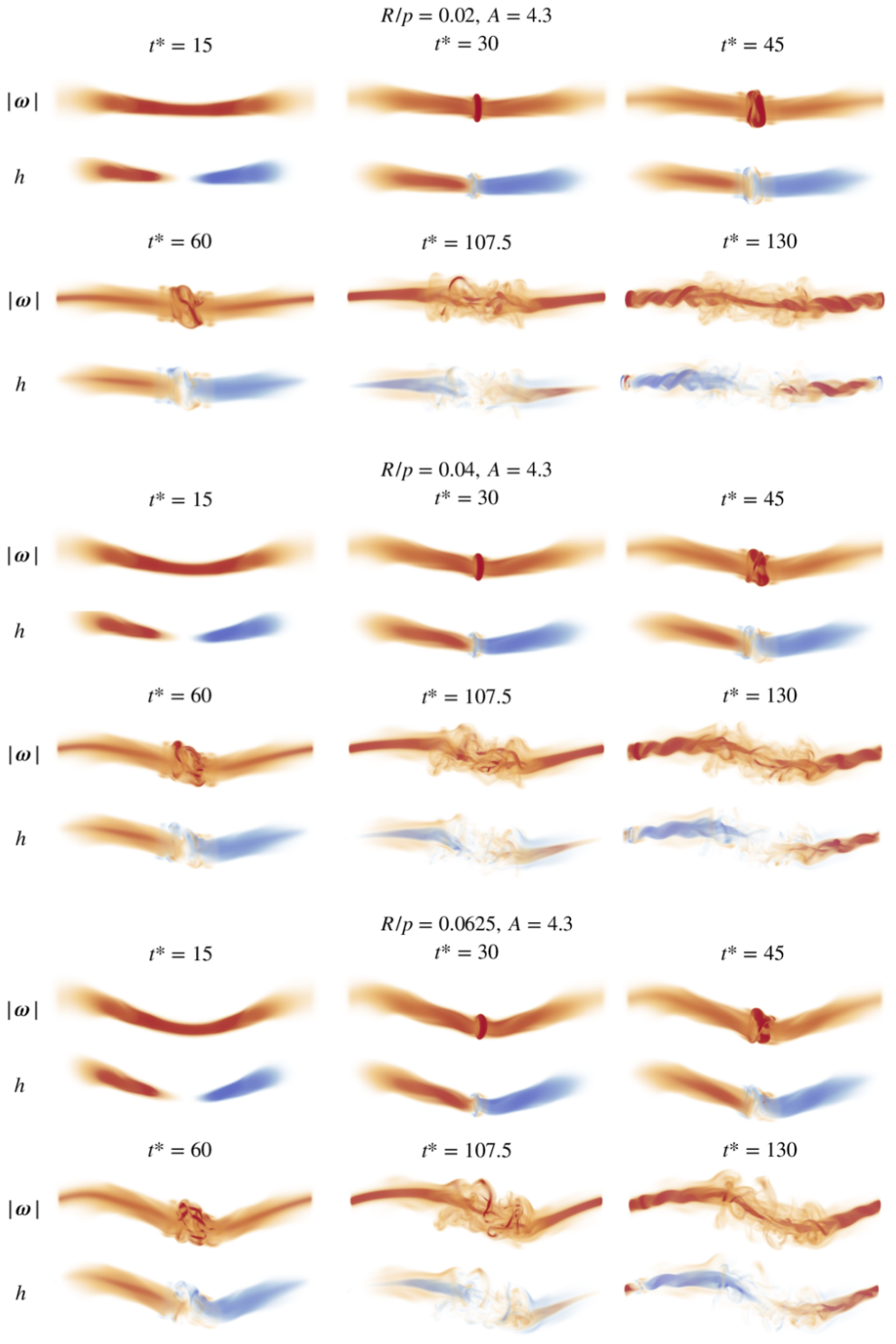

Figure 1: 3D volume rendering of vorticity magnitude $|\boldsymbol{\omega}|$ and helicity density $h = \boldsymbol{u} \cdot \boldsymbol{\omega}$ field for cases with different values of R/p and with $A = 3$ and $A = 4.3$ at different times. Colormaps same as in Fig. 3 in the main text.

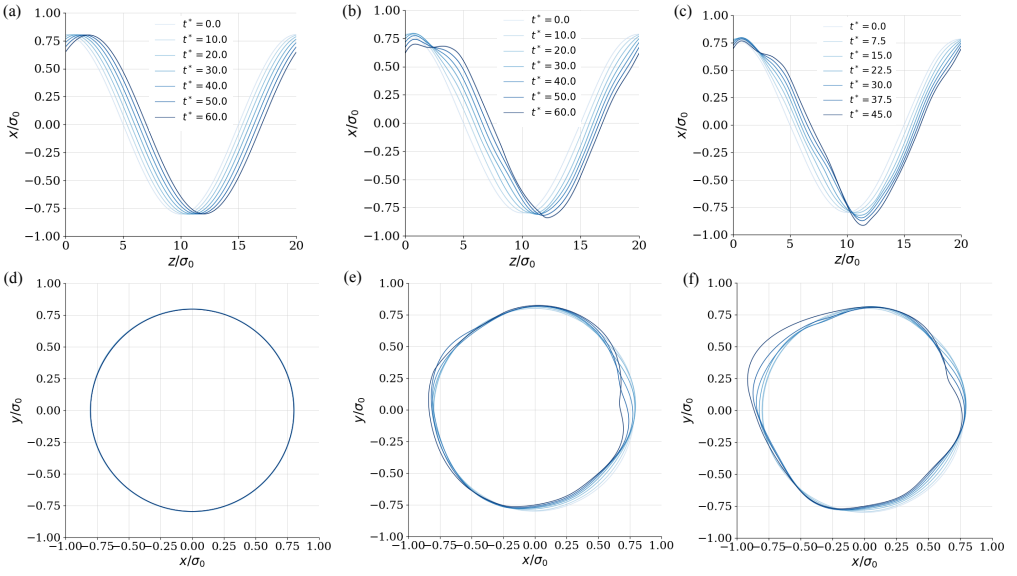

Figure 2: (a)–(c): Projection of the centerline l_c on the x-z plane for helical vortex case $A1.R4$, case $A3.R4$ and case $A4.R4$ at different times until the late stage of the primary bursting event (note the horizontal and vertical axes do not have the same scale). (d)–(f): Projection of the centerline l_c on the x-y plane for case $A1.R4$, case $A3.R4$ and case $A4.R4$, shown at the same times as (a)–(c).

2. Centerline of the helical vortex tube

We approximate the centerline of the helical vortex tube with the vorticity magnitude centroids on z slices (x-y planes with constant z) and denote the resulting line as l_c. For helical vortex tubes with core-size variations, during the early time before the first bursting event, the vortex tube appears to be relatively smooth and coherent and l_c is a good representation of the vortex centerline. However, during bursting, kinks appear in the bursting region, which indicate that the plane containing bursting structure is not perpendicular to the z axis. Nevertheless, it is possible to identify and ignore the region of bursting and interpolate over the remaining points to obtain a relatively smooth line as the axis of the vortex tube.

Fig. 2(a)–(c) show the x and z coordinates (or the projection of the vortex centerline on x-z plane) of the vortex centerline for an unperturbed helix case $A1.R4$ and helical tube case $A3.R4$ and case $A4.R4$ at different times till the late stage of the primary bursting. For the unperturbed helix case, we observe the centerline as a sinusoidal wave translating in the $+z$ direction, which reflects the self-induced rotational and translational motion of a helical vortex. For the helical tube with core-size variation, the projection of the centerline also translate in the $+z$ direction but it deviates from a sinusoidal shape, instead developing two separate peaks around $0 < z/\sigma_0 < 5$. This results from the propagation of the two opposite-signed twist waves away from the perturbed regions and the broken symmetry due to the self-induced axial flow.

Fig. 2(d)–(f) show the x and y coordinates (or the projection of the vortex centerline on x-y plane) for the same cases. For the unperturbed helix $A1.R4$, the projected curve for the centerline remains an axisymmetric circle, whereas for case $A3.R4$ and case $A4.R4$, the curves deviates from an axisymmetric shape as time evolves. This further demonstrates that twist wave propagation and bursting slightly deform the centerline of the helical vortex tube.

Case	$\overline{c}^*$	Δc^*	U_t^*	$U_{t,\mathrm{ref}}^*$
$A3.R0$	0.1856	0	0	0
$A4.R0$	0.2662			
$A3.R2$	0.1965	0.0018	0.00053	0.00039
$A4.R2$	0.2776	0.0019		
$A3.R4$	0.1978	0.0071	0.0019	0.00015
$A4.R4$	0.2755	0.0050		
$A3.R6$	0.1964	0.0181	0.0042	0.00032
$A4.R6$	0.2681	0.0106		

Table 1: The average of the left and right-handed twist wave speeds in lab frame $\overline{c}^* = \frac{1}{2}(c_L^* + c_R^*)$, their difference $\Delta c^* = c_R^* - c_L^*$, the self-induced velocity tangent to the centerline for the unperturbed helical tube denoted as U_t^*, and the theoretically predicted values for the tangent velocity at the centerline evaluated using Eqn. (2.18) in Fuentes (2017) $U_{t,\mathrm{ref}}^*$. All wave speeds and velocity components are non-dimensionalized with Γ_0/σ_0.

3. Left and right-propagating twist wave speed

In the SI of Ji & van Rees (2022), we discussed multiple ways of identifying the twist wave speed, all leading to similar results. Here we identify the twist wave front in the early time (before the first bursting) through the minimum of the tangent component of vorticity at the centerline, i.e. $\omega_t = \boldsymbol{\omega} \cdot \hat{\boldsymbol{e}}_t$ on l_c.

Similar to the straight tube case, each twist wave moves at an approximately constant speed during a time interval before bursting. We evaluate the speed of each twist wave through a linear fit of the twist wavefront position along the centerline over this time interval. The resulting non-dimensionalized wave speeds for the left- and right- propagating twist waves are listed in the Table. 1, written in terms of their average (first column) and difference (second column). The wave speeds are non-dimensionalized with Γ_0/σ_0. For reference, the third column shows the non-dimensional self-induced velocity tangent to the centerline measured on an unperturbed helical tube ($A = 1$) at $t^* = 30$, denoted as U_t^*. This shows that the twist wave propagation speed is several times larger than the self-induced tangential component of the axial velocity in all cases. Finally, the last column shows the tangential velocity $U_{t,\mathrm{ref}}^*$ for the helical vortex evaluated using Eqn. (2.18) in Fuentes (2017). This equation provides an explicit formula for the tangential component of velocity under the assumption of a uniform vortex core with core-size σ much smaller than the helix radius. In our case, these assumptions are violated but nevertheless we observe that U_t^* and $U_{t,\mathrm{ref}}^*$ are similar in magnitude and, more importantly, follow a similar trend in their increase with R/p.

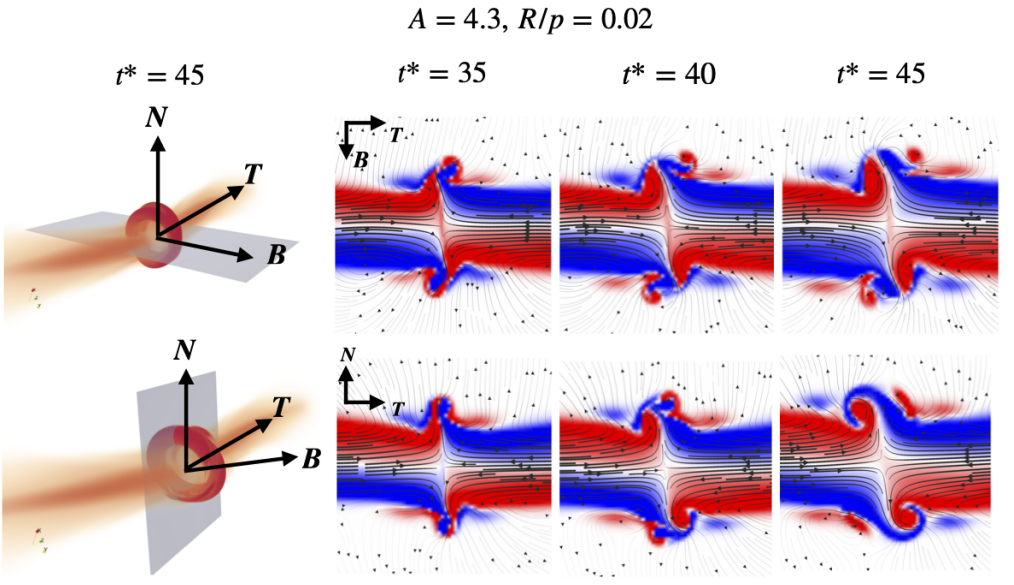

Figure 3: Probing the vorticity structure during bursting for case $A4.R2$. The left-most column shows the three-dimensional vorticity magnitude field and the semi-transparent planes are spanned by the tangent ($\boldsymbol{T}$) and binormal ($\boldsymbol{B}$) vectors, and the tangent ($\boldsymbol{T}$) and normal ($\boldsymbol{N}$) vectors, respectively. The last three columns show the corresponding vorticity component normal to the planes at different times. Colormap same as in Fig. 6 in the main text.

4. The vorticity structure during bursting for case $A4.R2$

Fig. 3 shows the planes spanned by $\boldsymbol{T}$ and $\boldsymbol{B}$ and $\boldsymbol{T}$ and $\boldsymbol{N}$ and the normal component of vorticity on these planes for case $A4.R2$, analogous to Fig. 6 for case $A3.R2$ in the main text.

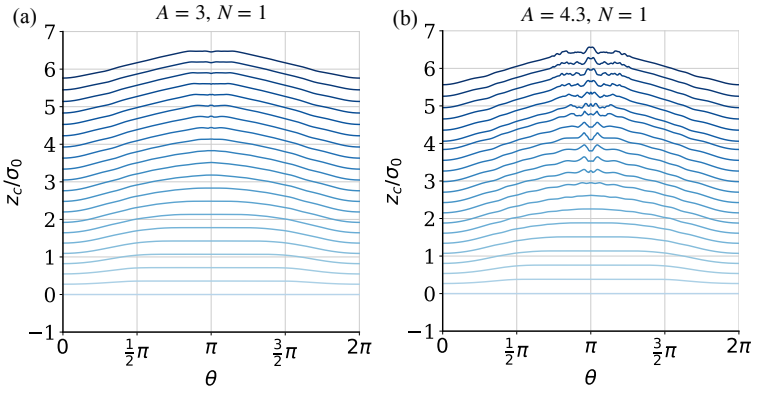

Figure 4: The z-component of the azimuthal vorticity centroid $z_c(\theta, t)$ for different values of θ at different times for (a) case $A3$ and (b) case $A4$ for $0 \leqslant t^* \leqslant 200$, with $\Delta t^* = 10$. The colors vary from light to dark as t^* increases.

5. Centerline distortion of the bursting vortex rings

Fig. 4 shows the z-component of the azimuthal vorticity centroid $z_c(\theta, t)$ for different values of θ at different times for the two vortex rings cases $A = 3$ and $A = 4.3$.

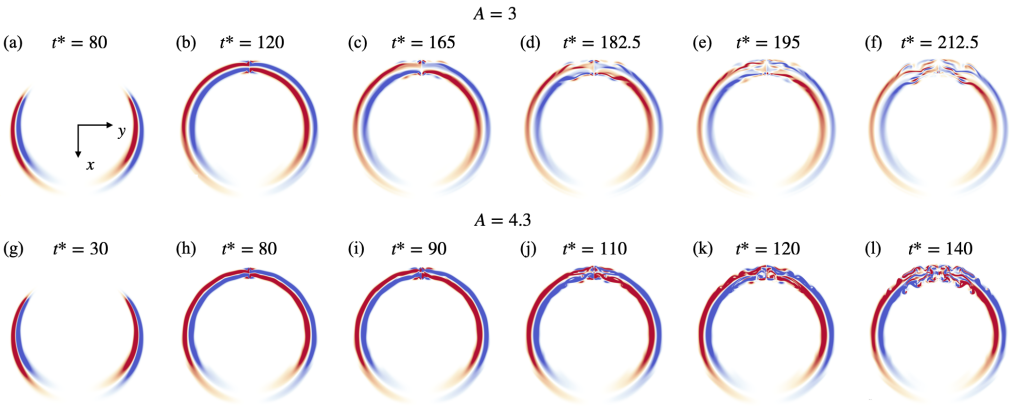

Figure 5: ω_z on the cross-sectional planes ($z = \overline{z}_c(t)$) at different times for case $A3$ (top row (a)-(f)) and case $A4$ (middle row (g)-(l)). Red indicates positive ω_z and blue indicates negative ω_z. Colormap same as in Fig. 13 in the main text.

6. Cross-sectional slice of the vertical vorticity component of the bursting vortex rings

Fig. 5 shows ω_z on $z = \overline{c}_z(t)$ planes at different times showing the entire rings for case $A3$ and $A4$. Fig. 13 in the main text shows a zoomed view of the bursting region for these cases.

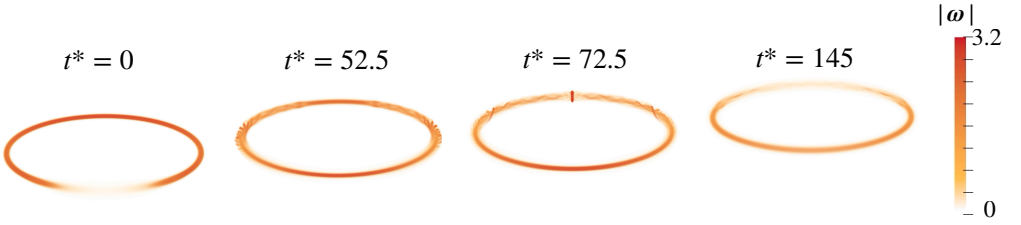

Figure 6: The vorticity magnitude field at different stages for the simulation of a vortex ring with smaller core-to-radius ratio $\frac{\sigma_0}{R} = 0.025$, $\frac{\lambda}{\sigma_0} = 10$, $A = 3$.

7. Effect of vortex ring core-to-radius ratio on bursting

To investigate the robustness of the presented results to a reduction in the core-to-radius ratio, we conducted an additional simulation of a core-size varying vortex ring with $\frac{\sigma_0}{R} = 0.025$, $\frac{\lambda}{\sigma_0} = 10$, $A = 3$. The results are compared with those in the main manuscript, where $\frac{\sigma_0}{R} = 0.1$ and all other non-dimensional parameters remain the same.

The simulation results show that the thin-cored ring undergoes qualitatively similar twist wave propagation and bursting events as the thicker core results in the main text. The vortex ring remains coherent with an approximately circular centerline, and no visible azimuthal centerline-displacement instability appears. However, some differences are also observed: the twist wave develops helical structures before the first bursting takes place, as shown in Fig. 6 ($t^* = 52.5$). This is different from the thicker core cases, where the core disintegrates only after the first bursting happens. A straightforward explanation is that for this case, the choice of non-dimensional parameters effectively yields an increase in the ring radius, thus the twist waves travel farther on a slightly less curved ring. Since the curvature is already large compared to the core radius, the effect of the slightly reduced curvature is minor, and instead the instability can be attributed to the increased time available for the unstable modes to develop and grow.

REFERENCES

Fuentes, Oscar Velasco 2017 Motion of a helical vortex. *Journal of Fluid Mechanics* **836**.

Ji, Lingbo & van Rees, Wim M. 2022 Bursting on a vortex tube with initial axial core-size perturbations. *Physical Review Fluids* **7** (4).